

Enhanced Hopping Conductivity in Low Band Gap Donor–Acceptor Molecular Wires Up to 20 nm in Length

Seong Ho Choi and C. Daniel Frisbie*

Department of Chemistry and Department of Chemical Engineering and Materials Science,
University of Minnesota, Minneapolis, Minnesota 55455, United States

Received August 7, 2010; E-mail: frisbie@umn.edu

Abstract: We have measured the current–voltage characteristics of conjugated oligo-tetrathiafulvalene-pyromelliticdiimide-imine (OTPI) wires ranging in length from 2.5 to 20.2 nm, contacted by Au electrodes. OTPI wires were built from Au substrates using alternating donor (tetrathiafulvalene, TTF) and acceptor (pyromelliticdiimide, PMDI) building blocks linked via aryl imine groups. Metal–molecule–metal junctions consisting of approximately 100 wires in parallel were prepared by contacting the wire films with an Au-coated atomic force microscope tip. The long OTPI wires exhibit a narrow band gap (<1.5 eV) and multiple redox states, which facilitate carrier injection from the Au contacts for hopping transport. We observe the theoretically predicted change in direct current (DC) transport from tunneling to hopping as a function of systematically controlled wire length, as well as strongly enhanced wire conductivity (0.02 S/cm) in the hopping regime. Hopping conduction is confirmed by length-, temperature-, and field-dependent transport measurements. These nanoscale transport measurements illuminate the role of molecular length and bond architecture on molecular conductivity and open opportunities for greater understanding of hopping transport in conjugated polymer films.

Introduction

The motivation for exploring the relationship between molecular structure and charge transport in metal–molecule–metal junctions lies in prospects for exploiting molecules in nano-electronics^{1–5} and in obtaining better understanding of conduction processes in molecular materials.^{6–9} Most prior molecular electronics experiments have focused on junctions that incorporate short molecules (<~4 nm) in which the junction transport mechanism is usually nonresonant tunneling. However, based on prior electron transfer experiments and theoretical considerations,^{10–18} it is well understood that the conduction mechanisms

in molecular junctions will depend on molecular length. When the molecules in the junction are long enough, and if the frontier orbitals are sufficiently well aligned with the electrode Fermi levels, charge hopping from source to drain electrodes will become more efficient than direct tunneling.

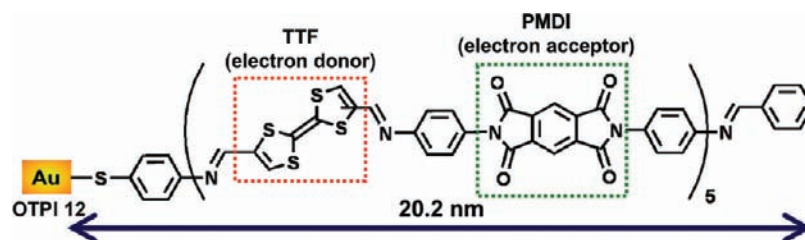
In the hopping regime, charge is injected from the source electrode into the molecules in the junction and is driven along the molecular length by the external electric field before it exits at the drain. This regime is much less explored than tunneling, and it has very different behavior in terms of the molecular length, temperature, and bias dependence of resistance.¹⁸ A goal for the field of molecular electronics is to understand structure–property relationships for hopping transport in molecular wires.^{7,19} Naturally, this goal requires reproducible methods for assembling long conjugated molecules between closely spaced contacts. In this regard, there has been significant recent progress using stepwise molecular synthesis combined with soft-contact approaches for completing the junctions.^{7,19}

Here, we report the synthesis and electrical characterization of long conjugated molecular wires with an alternating donor–acceptor architecture. Covalently bound donor–acceptor systems are known to have characteristically small HOMO–LUMO band gaps (<2.0 eV) as a result of donor and acceptor

- (1) Moth-Poulsen, K.; Bjornholm, T. *Nat. Nanotechnol.* **2009**, *4*, 551–556.
- (2) Kubatkin, S.; Danilov, A.; Hjort, M.; Cornil, J.; Bredas, J.-L.; Stuhr-Hansen, N.; Hedegard, P.; Bjornholm, T. *Nature* **2003**, *425*, 698–701.
- (3) Heath, J. R.; Ratner, M. A. *Phys. Today* **2003**, 43–49.
- (4) Park, J.; Pasupathy, A. N.; Goldsmith, J. I.; Chang, C.; Yaish, Y.; Petta, J. R.; Rinkoski, M.; Sethna, J. P.; Abruna, H. D.; McEuen, P. L.; Ralph, D. C. *Nature* **2002**, *417*, 722–725.
- (5) Diez-Perez, I.; Li, Z.; Hihath, J.; Li, J.; Zhang, C.; Yang, X.; Zang, L.; Dai, Y.; Feng, X.; Muellen, K.; Tao, N. *Nat. Commun.* **2010**, *1*, 1–5.
- (6) McCreery, R. L.; Bergren, A. J. *Adv. Mater.* **2009**, *21*, 4304–4322.
- (7) Choi, S. H.; Kim, B.-S.; Frisbie, C. D. *Science* **2008**, *320*, 1482–1486.
- (8) Li; Hihath, J.; Chen, F.; Masuda, T.; Zang, L.; Tao, J. *Am. Chem. Soc.* **2007**, *129*, 11535–11542.
- (9) Nitzan, A.; Ratner, M. A. *Science* **2003**, *300*, 1384–1389.
- (10) Segal, D.; Nitzan, A.; Davis, W. B.; Wasielewski, M. R.; Ratner, M. A. *J. Phys. Chem. B* **2000**, *104*, 3817–3829.
- (11) Segal, D.; Nitzan, A. *Chem. Phys.* **2001**, *268*, 315–335.
- (12) Berlin, Y. A.; Hutchison, G. R.; Rempala, P.; Ratner, M. A.; Michl, J. *J. Phys. Chem. A* **2003**, *107*, 3970–3980.
- (13) Grozema, F. C.; Siebbeles, L. D. A.; Warman, J. M.; Seki, S.; Tagawa, S.; Scherf, U. *Adv. Mater.* **2002**, *14*, 228–231.

- (14) Nitzan, A. *J. Phys. Chem. A* **2001**, *105*, 2677–2679.
- (15) Prins, P.; Grozema, F. C.; Schins, J. M.; Patil, S.; Scherf, U.; Siebbeles, L. D. A. *Phys. Rev. Lett.* **2006**, *96*, 146601.
- (16) Davis, W. B.; Svec, W. A.; Ratner, M. A.; Wasielewski, M. R. *Nature* **1998**, *396*, 60–63.
- (17) Weiss, E. A.; Ahrens, M. J.; Sinks, L. E.; Gusev, A. V.; Ratner, M. A.; Wasielewski, M. R. *J. Am. Chem. Soc.* **2004**, *126*, 5577–5584.
- (18) Nitzan, A. *Annu. Rev. Phys. Chem.* **2001**, *52*, 681–750.
- (19) Choi, S. H.; Risko, C.; Delgado, M. C. R.; Kim, B.; Bredas, J.-L.; Frisbie, C. D. *J. Am. Chem. Soc.* **2010**, *132*, 4358–4368.

Scheme 1. Molecular Structure of OTPI 12, the Longest OTPI Wire (20.2 nm)



orbital hybridization.^{20–32} Furthermore, low band gap conjugated polymers based on donor and acceptors exhibit many useful redox and optoelectronic properties,²¹ including broad and long wavelength light absorption,²² solid-state transport of both holes and electrons,²⁴ and access to multiple charge states in a small potential window.³³ These factors and the well-known conduction properties of donor–acceptor charge-transfer salts motivated us to build molecular wires based on donors and acceptors. Our expectation was that such systems would be more highly conducting than our previously reported wires.^{7,19}

We have used alternating tetrathiafulvalene (TTF) and pyromellitic diimide (PMDI) blocks to build oligo-tetrathiafulvalene-pyromellitic diimide-imine (OTPI) wires up to 20 nm in length, Scheme 1. These wires are significantly longer than our previous milestone of 10 nm,¹⁹ although they are about one-half the length of wires synthesized by Tuccitto et al.³⁴ using stepwise metal ion coordination chemistry. TTF was chosen as the donor building block because of its interesting and versatile electrochemical properties.³⁵ The electrochemical oxidation of the TTF ring system to the cation radical and closed-shell dication species occurs sequentially and reversibly within a very accessible potential window.³⁶ In addition, the TTF cation radical is thermodynamically very stable because the 1,3-dithiolium cation has 6 π -electron heteroaromaticity, which contributes to the strong donor behavior of TTF in many charge-transfer complexes. PMDI represents the smallest homologue of aromatic diimides that are a well-known class of acceptors and that have been of much interest for solar cells,³⁷ organic

field effect transistors,^{38–40} and solution electron transfer experiments.^{41,42} PMDI has a large electron affinity³⁸ (3.9 eV) and can interact with electron-rich π -systems such as TTF derivatives by inter-/intramolecular charge transfer.⁴³ In addition, both the TTF and the PMDI building blocks are unencumbered with bulky side groups, which facilitates the stepwise synthesis of molecular wires from metal electrodes.

We have grown OTPI wires from Au substrates using aryl imine addition chemistry that we and others have described previously.^{7,19,44} Low optical band gaps (<1.5 eV) are achieved in long OTPI wires as expected for alternating donor–acceptor systems. As wire length increases, multiple redox states are observed with a small potential gap (\sim 1.0 V) between the first oxidation and first reduction peak, which is consistent with the red-shift of the maximum UV–vis absorption for OTPI wires. Direct current (DC) conduction measurements using conducting probe atomic force microscopy (CP-AFM) reveal that there is a transition in transport mechanism from tunneling to hopping near 5 nm in length as evidenced by clear changes in the length, temperature, and electric field dependence of the current–voltage (I – V) characteristics. In longer OTPI wires, we estimate the wire conductivity is 0.02 S/cm, nearly 2 orders of magnitude higher than our previously reported wires.^{7,19} Overall, these results provide further evidence that stepwise aryl imine addition chemistry can be used to create a wide variety of molecular wire architectures and that the hopping regime can be reproducibly accessed and examined in molecular junctions. This work also demonstrates that the donor–acceptor motif does indeed lead to higher intramolecular DC conductivities. Furthermore, at up to 20 nm in length, the OTPI wires described here are the longest molecular wires to date to have been extensively electrically characterized.

Experimental Section

Materials. Au nuggets (99.999% pure) were purchased from Mowrey, Inc. (St. Paul, MN). Evaporation boats and Cr evaporation rods were obtained from R. D. Matthis (Long Beach, CA). Silicon (100) wafers were purchased from WaferNet (San Jose, CA). Contact mode AFM tips (DNP or NP silicon nitride probes) were purchased from Veeco Instruments (Camarillo, CA). Absolute ethanol was obtained from Fisher Scientific.

- (20) Roncali, J. *Chem. Rev.* **1997**, *97*, 173–206.
 (21) Segura, J. L.; Gomez, R.; Blanco, R.; Reinold, E.; Bauerle, P. *Chem. Mater.* **2006**, *18*, 2834–2847.
 (22) Peet, J.; Kim, J. Y.; Coates, N. E.; Ma, W. L.; Moses, D.; Heeger, A. J.; Bazan, G. C. *Nat. Mater.* **2007**, *6*, 497–500.
 (23) Gunbas, G.; Durmus, A.; Toppare, L. *Chem. Mater.* **2008**, *20*, 7510–7513.
 (24) Steckler, T. T.; et al. *J. Am. Chem. Soc.* **2009**, *131*, 2824–2826.
 (25) Martijn, M. W.; Mathieu, T.; Jan, G.; Ren, A. J. *J. Adv. Mater.* **2008**, *20*, 2556–2560.
 (26) Blouin, N.; Leclerc, M. *Acc. Chem. Res.* **2008**, *41*, 1110–1119.
 (27) Yongfang, L.; Yingping, Z. *Adv. Mater.* **2008**, *20*, 2952–2958.
 (28) Thompson, B. C.; Kim, Y.-G.; McCarley, T. D.; Reynolds, J. R. *J. Am. Chem. Soc.* **2006**, *128*, 12714–12725.
 (29) Kulkarni, A. P.; Zhu, Y.; Babel, A.; Wu, P.-T.; Jenekhe, S. A. *Chem. Mater.* **2008**, *20*, 4212–4223.
 (30) Usta, H.; Facchetti, A.; Marks, T. J. *J. Am. Chem. Soc.* **2008**, *130*, 8580–8581.
 (31) Liu, J.; Zhang, R.; Sauve, G. v.; Kowalewski, T.; McCullough, R. D. *J. Am. Chem. Soc.* **2008**, *130*, 13167–13176.
 (32) Beaujuge, P. M.; Ellinger, S.; Reynolds, J. R. *Nat. Mater.* **2008**, *7*, 795–799.
 (33) Alves, H.; Molinari, A. S.; Xie, H.; Morpurgo, A. F. *Nat. Mater.* **2008**, *7*, 574–580.
 (34) Tuccitto, N.; Ferri, V.; Cavazzini, M.; Quici, S.; Zhavnerko, G.; Licciardello, A.; Rampi, M. A. *Nat. Mater.* **2009**, *8*, 41–46.
 (35) Segura, J. L.; Martin, N. *Angew. Chem., Int. Ed.* **2001**, *40*, 1372–1409.
 (36) Bryce, M. R. *J. Mater. Chem.* **2000**, *10*, 589–598.
 (37) Tang, C. W. *Appl. Phys. Lett.* **1986**, *48*, 183–185.

- (38) Zheng, Q.; Huang, J.; Sarjeant, A.; Katz, H. E. *J. Am. Chem. Soc.* **2008**, *130*, 14410–14411.
 (39) Katz, H. E.; Lovinger, A. J.; Johnson, J.; Kloc, C.; Siegrist, T.; Li, W.; Lin, Y. Y.; Dodabalapur, A. *Nature* **2000**, *404*, 478–481.
 (40) Oh, J. H.; Lee, H. W.; Mannsfeld, S.; Stoltenberg, R. M.; Jung, E.; Jin, Y. W.; Kim, J. M.; Yoo, J.-B.; Bao, Z. *Proc. Natl. Acad. Sci. U.S.A.* **2009**, *106*, 6065–6070.
 (41) Bauer, P.; Wietasch, H.; Lindner, S. M.; Thelakkat, M. *Chem. Mater.* **2006**, *19*, 88–94.
 (42) Wasielewski, M. R. *Acc. Chem. Res.* **2009**, *42*, 1910–1921.
 (43) Hansen, J. G.; Bang, K. S.; Thorup, N.; Becher, J. *Eur. J. Org. Chem.* **2000**, 2135–2144.
 (44) Rosink, J. J. W. M.; Blauw, M. A.; Geerligs, L. J.; van der Drift, E.; Rousseeuw, B. A. C.; Radelaar, S.; Sloof, W. G.; Fakkeldij, E. J. M. *Langmuir* **2000**, *16*, 4547–4553.

Synthesis of Molecular Building Blocks. 4,4′(5′)-Diformyltetrathiafulvalene (DF-TTF) and *N,N*-di-(4-anilino)-1,2,4,5-benzenebis-(dicarboximide) (4-ABI) were synthesized as in the literature.^{45,46} However, we have followed a different workup procedure for DF-TTF to acquire higher yield. The reaction mixture based on 2 g of TTF starting material was added to 200 mL of H₂O, which was then extracted with 200 mL of CH₂Cl₂ in a separatory funnel. The organic layer was isolated, and the solvent was removed under pressure until the solution became almost saturated. The solvent was then dried, and the crude product was purified by column chromatography (silica gel, (CH₃)₂NC(O)H). The solvent was removed under pressure, and the solid was rinsed with copious amounts of methanol. The product was dried at room temperature, yielding 1.6 g (68%) of DF-TTF. The compound is a dark red solid mixture of (*E*) and (*Z*) isomers. Chromatographic separation of both isomers has not been achieved.

Growth and Characterization of Molecular Wires. The Au substrates were 1000 Å thick thin films on silicon (with a 50 Å Cr adhesion layer) prepared in a Balzers thermal evaporator at a rate of 1.0 Å/s at a base pressure of $\leq 2 \times 10^{-6}$ Torr. The metal surfaces were immersed in 10 mL of 1 mM 4-aminothiophenol (ATP) solutions in argon-purged absolute ethanol. A self-assembled monolayer (SAM) of ATP was grown for 18–24 h. After the sample was removed from the solution and immersed in absolute ethanol for 30 min to remove physisorbed molecules, the sample was immersed in 10 mL of 10 mM DF-TTF in chromatographic grade (CH₃)₂SO (dimethyl sulfoxide, DMSO) with 5 μL of HCl (37%) as an acid catalyst for 24 h. The sample was then immersed in pure DMSO for 1 h, and the same procedure was followed using 10 mM 4-ADI in DMSO. Lengths of the wires were controlled by the number of alternating additions of DF-TTF and 4-ABI. To finish the wire synthesis, odd and even OTPI wires were end-capped with benzaldehyde and aniline, respectively. All OTPI wires were rinsed with absolute ethanol and dried under a stream of N₂ before measurements.

OTPI wires were characterized by ellipsometry, X-ray photoelectron spectroscopy (XPS), reflection–absorption Fourier transform infrared spectroscopy (RAIRS), and cyclic voltammetry. Ellipsometry measurements were carried out on a VASE spectroscopic ellipsometer (J. A. Woollam Co., Inc.). Measurements of the polarization angles (Ψ and Δ) were taken as a function of wavelength (λ) between 600 and 1000 nm at an incident angle of 65° with respect to the surface normal. The indices of refraction ($n(\lambda)$) and extinction coefficients ($k(\lambda)$) of the Au-coated substrates were determined by measurement of the polarization angles prior to monolayer deposition and wire growth. The instrument software converted these values to $n(\lambda)$ and $k(\lambda)$ of Au films and saved them as a material file. After monolayer formation and wire growth on Au substrates, the polarization angles were measured again, and the film thicknesses were determined by a built-in algorithm. The $n(\lambda)$ and $k(\lambda)$ of the SAMs were assumed to be 1.45 and 0, respectively, over the wavelength range.

XPS spectra were taken on a Perkin-Elmer Phi 5400 spectrometer ($<10^{-9}$ Torr) with a Mg K α X-ray source (1253.6 eV) and a hemispherical analyzer. The X-ray anode was operated at 200 W, and the analyzer was set to a pass energy of 89.45 eV for survey scans and 17.9 eV for high-resolution scans. The binding energy scales were referenced to the Au_{4f7/2} peak (84.0 eV). SAM thicknesses were calculated using the relative intensities of the Au_{4f} and C_{1s} peaks and a hexadecanethiol SAM on Au as a reference ($d = 1.86$ nm). Assuming the same attenuation length of Au ($\lambda_{\text{Au}} = 3.36$ nm) and carbon ($\lambda_{\text{C}} = 2.27$ nm) photoelectrons for wire and hexadecane thiol monolayers, the calculation based on eq 1 yielded the thickness:

$$\frac{\frac{I_{\text{C}}}{I_{\text{Au}}}(\text{sample})}{\frac{I_{\text{C}}}{I_{\text{Au}}}(\text{reference})} = \frac{\left\{1 - \exp\left(-\frac{d_{\text{sample}}}{\lambda_{\text{C}}}\right)\right\} \exp\left(-\frac{d_{\text{reference}}}{\lambda_{\text{Au}}}\right)}{\exp\left(-\frac{d_{\text{sample}}}{\lambda_{\text{Au}}}\right) \left\{1 - \exp\left(-\frac{d_{\text{reference}}}{\lambda_{\text{C}}}\right)\right\}} \quad (1)$$

where I_{C} is the integrated intensity of the C_{1s} peaks, I_{Au} is the integrated intensity of the Au_{4f} peaks, and d is the thickness.

Reflection–absorption infrared spectroscopy (RAIRS) were collected with a Nicolet Series II Magna-750 FTIR with a Harrick Seagull accessory for grazing angle specular reflectance measurements. The infrared beam was incident at 84° with respect to the surface normal. A total of 2000 scans were collected at 1.0 cm⁻¹ resolution. RAIRS was used for monitoring stepwise imination, Figure 1b. Cyclic voltammetry (CV) experiments were undertaken to determine the redox states of OTPI wires and to measure surface coverage. In these experiments, a three-neck electrochemical cell was used. A clean O-ring (1.0 cm diameter) in a cylindrical cavity surrounding a hole in the bottom of the cell was placed between the cell and a monolayer-coated Au substrate, which acted as the working electrode. The cell was filled with 0.2 M [Bu₄N⁺][PF₆⁻] (tetrabutylammonium hexafluorophosphate) in purified CH₃CN, which was deoxygenated by three cycles of freeze–pump–thaw treatments. A Pt wire was used as the counter electrode, and the cell was referenced to an oxidized Ag wire. Prior to examining the monolayer oxidation potentials, the system was calibrated to the ferrocene oxidation potential. For each monolayer, the scan was recorded at a sweep rate of 100 mV/s, and the CV curves were reproducible and stable to electrochemical cycling within the range of –2.0 to +1.5 V vs Ag wire. The surface coverage (Γ) was determined according to eq 2:

$$\Gamma = \frac{Q}{nFA} \quad (2)$$

where Q is the charge injected into the SAM, n is the number of electrons involved in the electron-transfer process, F is the Faraday constant, and A is the surface area of the monolayer examined, that is, the area inside of the O-ring. Q was obtained by integrating the area under the first peak in the forward sweep of the cyclic voltammogram.

Determination of Optical Band Gaps. The electronic structures of OTPI wires were examined by UV–visible spectroscopy. UV–visible absorption spectra were taken of the molecular films on semitransparent thin Au films using a Beckman Coulter DU720 UV–visible spectrometer. Twenty nanometer thick Au films were thermally deposited on a plastic UV cell, which had solvent resistance to DMSO. Molecular films were formed on the Au film in the same manner described above.

Junction Formation and Current–Voltage Measurements by CP-AFM. Molecular junctions were formed by bringing an Au-coated tip into contact with a wire monolayer, as illustrated in the inset of Figure 6a. These experiments were performed with a Multimode AFM (Veeco Instruments) in a glovebox (O₂ < 8 ppm). A 1 nN load force was used to make reproducible contact. Au-coated tips were prepared as reported previously.⁴⁷ We have examined the current–voltage (I – V) characteristics of OTPI wires over ± 0.2 V for OTPI 1, ± 0.5 V for OTPI 2, ± 1.0 V for OTPI 3–5, and ± 1.5 V for OTPI 6–12. The low voltage resistance was determined from the linear I – V relationship within the range of ± 0.05 V. Four Au-coated AFM tips having a radius of ~ 50 nm were used for the measurements, each of which gave the same resistance value, $(6 \pm 0.2) \times 10^8 \Omega$, for tunneling through an octanethiol SAM (an effective calibration standard). The four tips were used separately to examine three sets of wires: OTPI 1–3

(45) Andreu, R.; Garin, J.; Orduna, J. *Tetrahedron Lett.* **1994**, *35*, 9243–9246.

(46) Neuber, C.; Bate, M.; Giesa, R.; Schmidt, H.-W. *J. Mater. Chem.* **2006**, *16*, 3466.

(47) Engelkes, V. B.; Beebe, J. M.; Frisbie, C. D. *J. Phys. Chem. B* **2005**, *109*, 16801–16810.

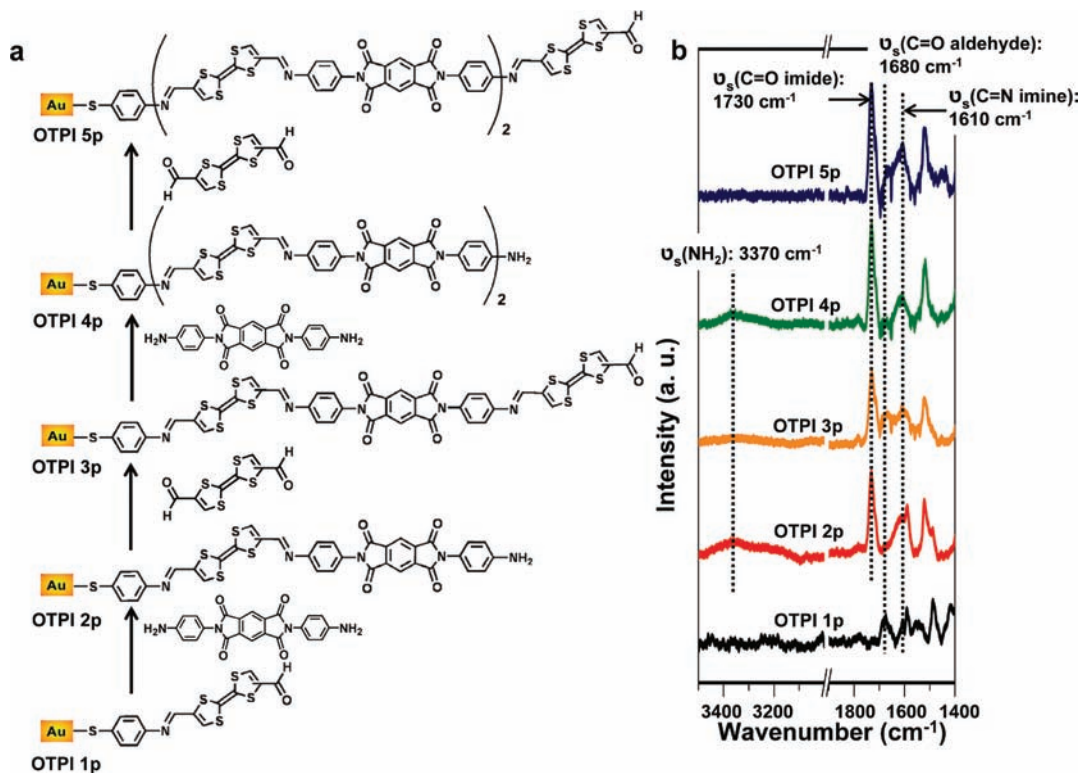


Figure 1. (a) Molecular structure and synthetic route to precursor wires, OTPI-*p*, on Au substrates. The first five reaction steps are shown. (b) RAIRS spectra of OTPI-*p* monolayers.

(tip 1), OTPI 3–7 (tip 2), OTPI 7–10 (tip 3), and OTPI 10–12 (tip 4). Note that OTPI 3, 7, and 10 were each measured with two different tips to confirm that the same resistances were obtained. The number of molecules in each junction was estimated on the basis of the tip radius and the wire surface coverage to be ~ 100 (corresponding to a contact area of ~ 50 nm²).

Variable temperature measurements of the OTPI wire resistances were performed with an environmentally controlled Molecular Imaging PicoScan/PicoSPM. We have checked that the tunneling current of the octanethiol SAM remains constant within our experimental uncertainty⁴⁸ from -30 °C (243 K) to room temperature at $<5\%$ RH. Two different sample stages, a normal heating stage and a Peltier stage, were used to vary temperature above and below room temperature, respectively. Ag paste was painted at the edge of each sample to make thermal contact between the sample and stage. The measured temperatures on the samples were consistent with the set point temperatures. The resistances were determined from linear I – V relationships within the range of ± 1 mV for OTPI 1, ± 5 mV for OTPI 2, and ± 0.05 V for OTPI 3, 6, 9, and 12, and they are the average values of resistances obtained at six different locations on the samples. Note that the maximum current is limited to ± 10 nA for our variable temperature setup. For OTPI 1, we placed a 100 k Ω ($\pm 0.1\%$ tolerance) resistor in series with the junction to force currents stay within the detection limits over the ± 1 mV voltage range. Two Au-coated AFM tips having a radius of ~ 50 nm were used for the measurements, each of which gave the same resistance value for tunneling through an octanethiol SAM and OTPI 2. The two tips were used separately to examine the resistances of OTPI 1, 2, 3, 6, 9, and 12 in two temperature ranges: 245–293 K (tip 1) and 303–333 K (tip 2).

All measurements were performed while keeping the relative humidity of the instrument chamber below 5%.

Results and Discussion

Growth and Characterization of Molecular Wires. OTPI wires were prepared from a Au substrate using the aryl imine chemistry with alternate addition of 4,4′(5′)-diformyltetra-thiafulvalene (DF-TTF) and *N,N*-di-(4-anilino)-1,2,4,5-benzene-bis(dicarboximide) (4-ABI). Figure 1a shows the molecular structure and synthetic routes for OTPI wire precursors (OTPI-*p*) up to the fifth addition step. The molecular structures for longer wires are shown in Figure S1. Each OTPI-*p* wire terminated with $-\text{NH}_2$ or $-\text{CHO}$ groups was end-capped with benzaldehyde or aniline, respectively. The end-capping provided a consistent terminal group throughout the OTPI series that facilitated reproducible electrical characterization.

The growth of wires was monitored using reflection–absorption Fourier transform infrared spectroscopy (RAIRS). The RAIRS data, shown in Figure 1b, reveal the alternate appearance and disappearance of carbonyl stretches (1680 cm^{−1}) in the aldehyde terminal group and symmetric amine stretches (3370 cm^{−1}) in OTPI-*p* molecules up to 5 (Figure 1b) and 12 addition steps (Figure S1), which verifies the imination mechanism and indicates roughly quantitative reaction of all exposed reactive end groups. The intensity of imine stretching (1610 cm^{−1}) and the benzene ring vibrational mode (~ 1500 cm^{−1}) also increased with the number of repeat units, as expected. In addition, the intensity of the imide carbonyl stretches (1730 cm^{−1}) increased with the number of PMDI units incorporated into the OTPI wires. Complete end-capping was confirmed by the disappearance of the terminal group vibrational modes as shown in Figure S1.

(48) Kwatra, B.; Ramakrishna, V.; Suri, S. K. *Thermochim. Acta* **1981**, *48*, 231–235.

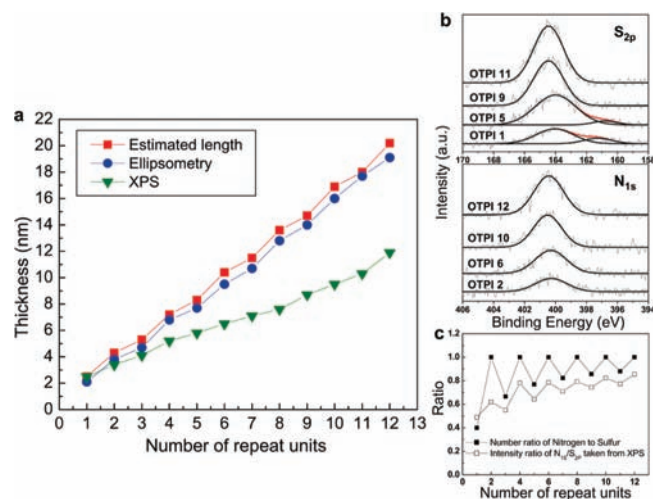


Figure 2. (a) The measured thicknesses and estimated lengths for OTPI wires as a function of the number of repeats. Blue circles and green triangles indicate the measured thicknesses, respectively, by ellipsometry and XPS. The estimated lengths are represented in red squares and were obtained with the Cambridge Scientific Chem3D software. Molecular length is the terminal H to S distance plus the Au–S bond length. It was assumed that the Au–S bond length is 2.36 Å. (b) High resolution XPS spectra in the S 2p region (top) and the N 1s region (bottom) for selected OTPI wires with different lengths. In each scan, light gray lines represent experimental data, and black and red lines show individual peak contributions and overall fit, respectively. (c) Calculated number ratio of N to S as function of the repeat units for OTPI wires (■), and measured N to S ratios determined from the peak areas of the N 1s and S 2p core-level spectra, corrected for atomic sensitivity factors (□).

The OTPI monolayers were extensively characterized by ellipsometry, X-ray photoelectron spectroscopy (XPS), cyclic voltammetry (CV), and UV–vis spectroscopy. Key results are shown in Figures 2–4 and are compiled in Table 1. Figure 2a shows the estimated molecular length and the measured thickness by ellipsometry and XPS for all OTPI wires. The monolayer thicknesses determined from ellipsometry are well correlated with the estimated length, indicating that OTPI wires have grown in an upright (essentially untilted) orientation as wire length increases up to 20 nm. However, the XPS thickness measurements are consistently lower, although they increase monotonically with the number of repeat units, as expected. The thicknesses measured by XPS are likely systematically underestimated because only the relative intensity of C 1s to Au 4f photoelectrons was taken into account in eq 1 and no corrections in the attenuation factors λ_C or λ_{Au} were made to account for the significant concentrations of S, N, and O in the SAMs. However, both ellipsometry and XPS indicate that the wire length increases with the number of repeat units.

XPS was also employed to record high resolution scans of the S_{2p} and N_{1s} regions. The photoelectron intensity emitted from these heteroatoms increased with the number of repeat units as shown in Figure 2b, which is consistent with the synthesis scheme in Figure 1a. We fit each high resolution spectrum using a combination of Gaussian and Lorentzian line shapes. In particular, the S 2p spectra for shorter OTPI wires (up to fifth layer) were deconvoluted to a pair of peaks at 164 and 161 eV, which represent S in TTF and the thiol surface-linking group, respectively. As expected, the S_{2p} spectra at ~161 eV are less distinct for longer wires because of the intensity attenuation of the Au-bonded thiol. The N high resolution scan reveals the imine and imide N. Importantly, one can also see in Figure 2c that the intensity ratio of N/S alternates with sequential additions

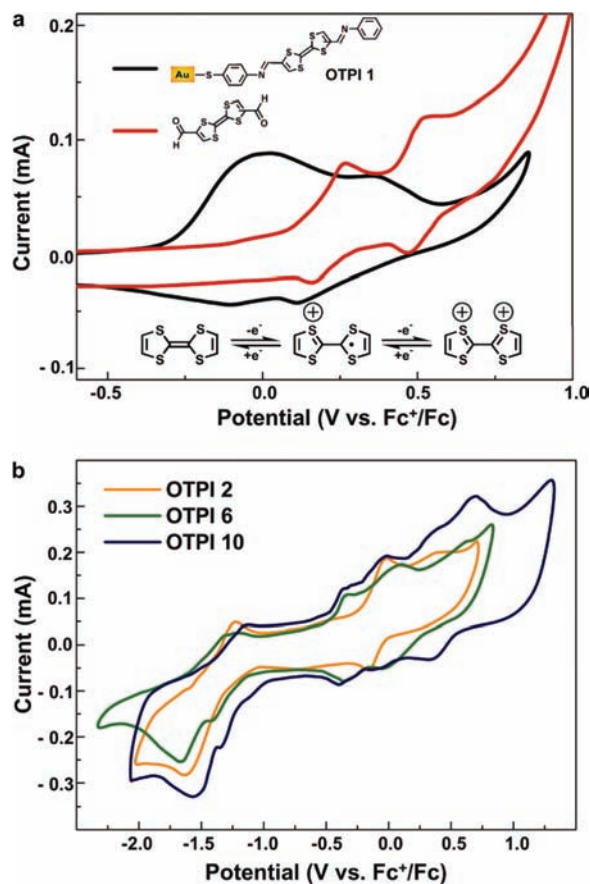


Figure 3. (A) Cyclic voltammograms of OTPI 1 wires on Au and of the DF-TTF building block in solution. (B) Cyclic voltammograms of OTPI 2, 6, and 10 on Au. The electrolyte was [Bu₄N⁺][PF₆⁻] (tetrabutylammonium hexafluorophosphate) in CH₃CN. The reference and counter electrodes were Ag wire and Pt gauze, respectively. The scan rates were 100 mV/s.

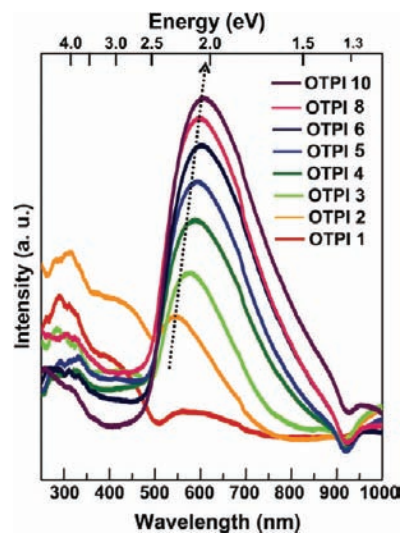


Figure 4. UV–vis absorption spectra of selected OTPI wires. The dashed arrow indicates the increase of the maximum absorption wavelength with wire length. UV–vis spectra of OTPI 11 and 12 are not available because the Au layer on the plastic cuvette became unstable over the long period of wire growth (>260 h) in DMSO solution.

of N-rich PMDI and S-rich TTF, which is also consistent with the chemistry shown in Figure 1a.

Cyclic voltammograms (CV) of selected OTPI wires are displayed in Figure 3. The potentials of the first oxidation/

Table 1. Redox Properties and Energy Level Alignments of OTPI Wires^a

monolayer	molecular length (nm)	first oxidation potentials, $E_{\text{ox}}^{\text{1st}}$ (V)	first reduction potentials, $E_{\text{red}}^{\text{1st}}$ (V)	surface coverage ($\times 10^{-10}$ mol/cm ²)	$\Delta E_{\text{HOMO-LUMO}}$ (V)	E_g (eV)
OTPI 1	2.5	-0.07		5.1		1.70
OTPI 2	4.3	-0.09	-1.69	5.6	1.60	1.59
OTPI 3	5.3	-0.13	-1.65	4.9	1.52	1.53
OTPI 4	7.2	-0.15	-1.55	3.8	1.40	1.36
OTPI 5	8.3	-0.21	-1.55	4.2	1.34	1.36
OTPI 6	10.4	-0.28	-1.45	3.4	1.17	1.35
OTPI 7	11.5	-0.30	-1.45	3.1	1.15	1.35
OTPI 8	13.6	-0.30	-1.41	3.2	1.11	1.35
OTPI 9	14.7	-0.32	-1.39	2.9	1.07	1.32
OTPI 10	16.9	-0.31	-1.36	2.6	1.05	1.30
OTPI 11	18.0	-0.34	-1.32	2.8	0.98	
OTPI 12	20.2	-0.35	-1.32	2.1	0.97	

^a Redox potential differences ($\Delta E_{\text{HOMO-LUMO}}$) were determined from the potential gap of the first oxidation/reduction peak (peak-to-peak) for OTPI wires, referenced to ferrocenium/ferrocene (Fc^+/Fc). The optical gap (E_g) was obtained from the edge of UV–visible absorption.

reduction states and the estimated surface coverage for each OTPI wire are tabulated in Table 1. For OTPI 1, no reduction was detected within the solvent electrochemical window. For longer OTPI wires that incorporate electron acceptor units (PMDI blocks), all oxidation and reduction peaks were reversible within the range of -2.0 to +0.8 V versus ferrocenium/ferrocene (Fc^+/Fc). As we noted in the Introduction, TTF is a reversible, stable two-electron donor (see the inset scheme in Figure 3a). Two reversible oxidation peaks were thus observed with OTPI 1 as shown in Figure 3a. In addition, these peaks shifted by -0.4 V as compared to the solution voltammetry of DF-TTF (the red line in Figure 3a), which is largely expected on the basis of the increased conjugation length upon formation of OTPI 1 and the removal of the aldehyde electron-withdrawing groups.

Once PMDI moieties were incorporated in the molecular backbone (after OTPI 2), reduction features appeared within the stable potential window as displayed in Figure 3b. The potential gap between the first oxidation and reduction, an electrochemical band gap ($\Delta E_{\text{HOMO-LUMO}}$), was significantly reduced from 1.6 to 1.0 V as wire lengths increased (Figure 3b and Table 1), which is consistent with increased conjugation of the system.

As shown in Figure 3b, multiple charge states (four oxidations and two reductions) are accessible for OTPI 10 inside the 3 V potential window, whereas two oxidations and one reduction are observed for OTPI 2 within the same window. The surface coverage obtained from the first oxidation peak is nearly identical over the entire set of wires (2.1×10^{-10} to 5.6×10^{-10} mol/cm²). These surface coverage data indicate that the number of molecular wires contacted by the electrodes in junction experiments varies by a factor of 2 or so. Collectively, the ellipsometry, XPS, and cyclic voltammetry data indicate that the oligoimine addition chemistry can be employed to prepare good quality monolayers of the OTPI wires.

Figure 4 displays the UV–vis absorption spectra for selected OTPI wires. As established with a variety of donor–acceptor polymers and charge-transfer complexes,^{20–24,49} the absorption for OTPI wires spans a broad wavelength range, and the onset begins at wavelengths as long as 925 nm, which reveals the small optical band gap as low as 1.3 eV. Optical band gaps

(E_g) for each OTPI wire were deduced from the onset of the lowest absorption band and are listed in Table 1. The E_g values are somewhat larger than the redox potential differences ($\Delta E_{\text{HOMO-LUMO}}$) determined from CV sweeps for OTPI 5 and longer wires. Disparity between electrochemical and optical band gaps (smaller $\Delta E_{\text{HOMO-LUMO}}$ than E_g) is often reported in many donor–acceptor dyads based on TTF and aromatic diimides,^{50–52} although the observation is not well explained. By density functional theory (DFT) calculations of the HOMO and LUMO levels of dibenzo-TTF bisimides, Gao et al.⁵³ reported that the largest coefficients for the HOMO are located mainly on the central TTF core, whereas the coefficients for the LUMO are mostly localized on the two imide rings. Close spatial proximity between HOMO and LUMO orbital density is an important factor in determining the band gap.⁵² We hypothesize that the optical transition we measure for OTPI wires does not correspond to the HOMO–LUMO transition but perhaps to the HOMO–1 or HOMO–2 to LUMO transition in which spatial overlap of the orbitals (and thus the transition dipole) is improved.^{51,54} Confirmation will of course require quantum chemical modeling.

The most important observation regarding the UV–vis spectra is that the absorption peaks and edges shift to longer wavelength as wire lengths increase (2.3 to 1.9 eV, see the dotted arrow in Figure 4). This strong bathochromic shift with increasing wire length was not observed with our previous wires based on phenylene imines⁷ and naphthalene/fluorene imines,¹⁹ in which electronic delocalization extended only over three repeating units because of their twisted conformations. OTPI wires perhaps have more planar conformations and thus more conjugation than the previous wires in part because the five-membered ring in TTF has less steric interaction with imine bonds than phenylene rings. Intermolecular interactions in the SAMs may also help enforce planarity of the wires.

Electrical Characterization of OTPI Wires (Low Bias). Length-Dependent Resistance. We investigated the transport characteristics of OTPI wires using CP-AFM (inset Figure 5a), a technique that has been employed to measure conduction in a variety of molecular systems.^{55–58} The resistance was determined using Au-coated AFM tips in contact with the OTPI wires grown on Au substrates. An I – V sweep of OTPI wires generally yielded a sigmoidally shaped curve as will be shown later, but over a small voltage range (± 0.05 V) the response was linear. The resistances shown in Figure 5 are low voltage resistances determined over this small voltage range and averaged for 20 I – V traces. Figure 5a shows a semilog plot of resistance (R) versus molecular length (L) for the entire set of

(49) Beaujuge, P. M.; Ellinger, S.; Reynolds, J. R. *Nat. Mater.* **2008**, *7*, 795–799.

- (50) Jaggi, M.; Blum, C.; Dupont, N.; Grilj, J.; Liu, S.-X.; Hauser, J. r.; Hauser, A.; Decurtins, S. *Org. Lett.* **2009**, *11*, 3096–3099.
- (51) Jaggi, M.; Blum, C.; Marti, B. S.; Liu, S.-X.; Leutwyler, S.; Decurtins, S. *Org. Lett.* **2010**, *12*, 1344–1347.
- (52) Perepichka, D. F.; Bryce, M. R.; Pearson, C.; Petty, M. C.; McInnes, E. J. L.; Zhao, J. P. *Angew. Chem., Int. Ed.* **2003**, *42*, 4636–4639.
- (53) Gao, X.; Wang, Y.; Yang, X.; Liu, Y.; Qiu, W.; Wu, W.; Zhang, H.; Qi, T.; Liu, Y.; Lu, K.; Du, C.; Shuai, Z.; Yu, G.; Zhu, D. *Adv. Mater.* **2007**, *19*, 3037–3042.
- (54) Bendikov, M.; Wudl, F.; Perepichka, D. F. *Chem. Rev.* **2004**, *104*, 4891–4946.
- (55) Beebe, J. M.; Kim, B.-S.; Frisbie, C. D.; Kushmerick, J. G. *ACS Nano* **2008**, *2*, 827–832.
- (56) Kim, B.-S.; Beebe, J. M.; Jun, Y.; Zhu, X. Y.; Frisbie, C. D. *J. Am. Chem. Soc.* **2006**, *128*, 4970–4971.
- (57) Engelkes, V. B.; Frisbie, C. D. *J. Phys. Chem. B* **2006**, *110*, 10011–10020.
- (58) Beebe, J. M.; Kim, B.-S.; Gadzuk, J. W.; Frisbie, C. D.; Kushmerick, J. G. *Phys. Rev. Lett.* **2006**, *97*, 026801.

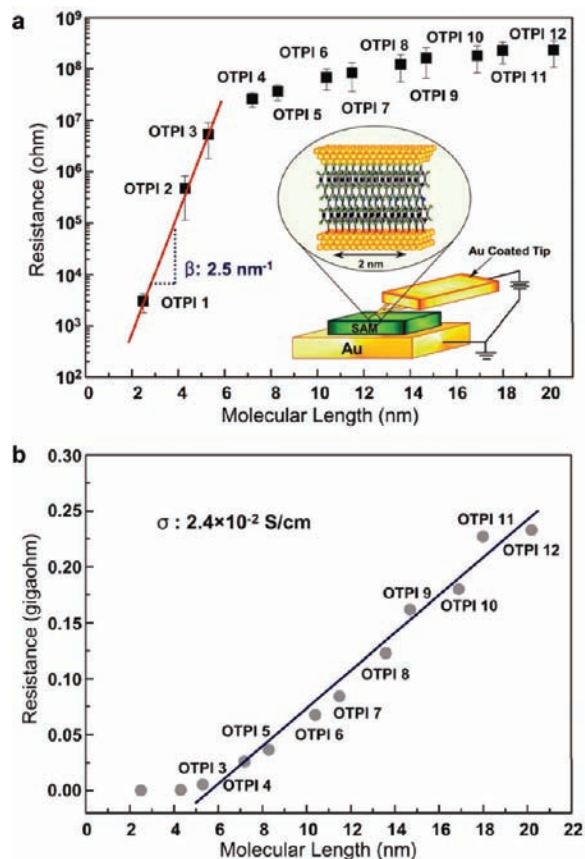


Figure 5. Measurements of molecular wire resistance with conducting probe atomic force microscopy (CP-AFM). (a) Semilog plot of R versus L for the Au/wire/Au junctions. Each data point is the average differential resistance obtained from 20 I - V traces in the range -0.05 to $+0.05$ V. Error bars represent one standard deviation. The straight line is a linear fit to the data according to eq 3. Inset: An Au-coated tip was brought into contact with an OTPI monolayer on an Au substrate. (b) A linear plot of R versus L for the Au/wire/Au junctions. The straight line is a linear fit to the data and yields the conductivity using an estimated tip/wire contact area of 25 nm^2 .

OTPI wires. A clear transition in length dependence of resistance is evident near 5 nm, which indicates a change in transport mechanism as we have seen previously in other wires.^{7,19} While resistances for short wires (OTPI 1–3) increase exponentially with length, resistances in long wires (OTPI 3–12) are much less sensitive to the wire lengths. For short wires, the exponential increase of resistance is consistent with the nonresonant tunneling process, described by

$$R = R_0 \exp(\beta L) \quad (3)$$

where R is the junction resistance, R_0 is the effective contact resistance, L is molecular length, and β is the tunneling attenuation factor that depends on the nature of bonding in the molecular backbone and the position of the junction Fermi level with respect to the frontier orbitals. The β value obtained from a linear fit to the data is $2.5 \pm 0.5 \text{ nm}^{-1}$, within the range of β values observed in typical conjugated systems.^{6,59,60}

For long wires, the resistances depend linearly on molecular length as shown in a plot of R versus L (Figure 5b), which

indicates that hopping transport prevails in these wires.^{18,61} Importantly, the wire conductivity estimated from the slope in the linear fit of Figure 5b is $2.4 \times 10^{-2} \text{ S/cm}$, more than 2 orders of magnitude higher than our previously reported oligoimine wires ($\sim 1.0\text{--}1.8 \times 10^{-4} \text{ S/cm}$).^{7,19} There may be several causes for this larger conductivity. First, significant lowering of the optical band gap and multiple redox states associated with the donor–acceptor architecture allows either holes or electrons to be readily injected into OTPI wires; that is, potential barriers to injection are likely to be smaller in these low band gap wires. Second, the conjugation length continues to increase over 10 repeat units for OTPI wires (see Figure 4), spanning $\sim 17 \text{ nm}$, which is consistent with a more planar configuration of the OTPI wires and more electronic delocalization, and this should also aid hopping transport. We observe a significantly smaller activation energy for hopping in the OTPI wires (see below), which supports the concept that the wires have a more favorable electronic structure for transport than our previously reported systems.

Third, there is an experimental detail that may also affect the conductivity results. The CP-AFM technique requires the use of a laser beam to monitor the cantilever deflection during the measurement. In our current setup, this laser emits at 680 nm, well within the absorption peak of the long OTPI wires. Thus, optical excitation may result in the generation of carriers in the OTPI molecules to a much greater degree than for wires we have previously examined.^{7,19} We note it is possible to modify the CP-AFM setup to incorporate a longer wavelength laser (900 nm), and this will allow systematic comparison of conductivity under visible versus near-infrared illumination.

Temperature-Dependent Resistances. Although a change in transport mechanism is apparent in the R versus L plot, the temperature dependence is key to verifying different transport mechanisms. Figure 6 shows an Arrhenius plot of $\log(R)$ versus $1/T$ for selected OTPI wires. The associated I - V curves are given in Figure S2. Clearly, the resistance for OTPI 1 is independent of temperature from 246 to 333 K, as expected for tunneling. For OTPI 2, the resistances are somewhat dependent on temperature; that is, the resistances from 313 to 333 K exhibit activated behavior with an activation energy of 0.45 eV, but there is a transition to weaker temperature dependence below 298 K. This transition may represent a change in charge transport from hopping at high temperature to tunneling at low temperature. Selzer et al.^{62,63} observed a similar characteristic transition at very low temperature ($\sim 100 \text{ K}$) in molecular junctions incorporating individual molecules of 1-nitro-2,5-di(phenylethynyl-4'-mercapto) benzene (NDB). OTPI 2 appears to be an unusual case in that it displays both activated and activationless transport depending on the temperature range. Around room temperature, however, the transport mechanism in OTPI 2 is most likely tunneling.

OTPI 3 and longer wires (OTPI 6, 9, and 12) display strongly thermally activated transport, characteristic of hopping, as shown in Figure 6. The activation energies (E_a) determined from the slopes are smaller (0.27 eV or 6.3 kcal/mol) for longer wires (OTPI 9 and 12) than for shorter wires (0.41 eV or 9.5 kcal/mol for OTPI 3 and 6). The 140 meV difference of the hopping

(61) Segal, D.; Nitzan, A.; Ratner, M.; Davis, W. B. *J. Phys. Chem. B* **2000**, *104*, 2790–2793.

(62) Selzer, Y.; Cabassi, M. A.; Mayer, T. S.; Allara, D. L. *J. Am. Chem. Soc.* **2004**, *126*, 4052–4053.

(63) Selzer, Y.; Cai, L.; Cabassi, M. A.; Yao, Y.; Tour, J. M.; Mayer, T. S.; Allara, D. L. *Nano Lett.* **2005**, *5*, 61–65.

(59) McCreery, R. L. *Chem. Mater.* **2004**, *16*, 4477–4496.

(60) Salomon, A.; Cahen, D.; Lindsay, S.; Tomfohr, J.; Engelkes, V. B.; Frisbie, C. D. *Adv. Mater.* **2003**, *15*, 1881–1890.

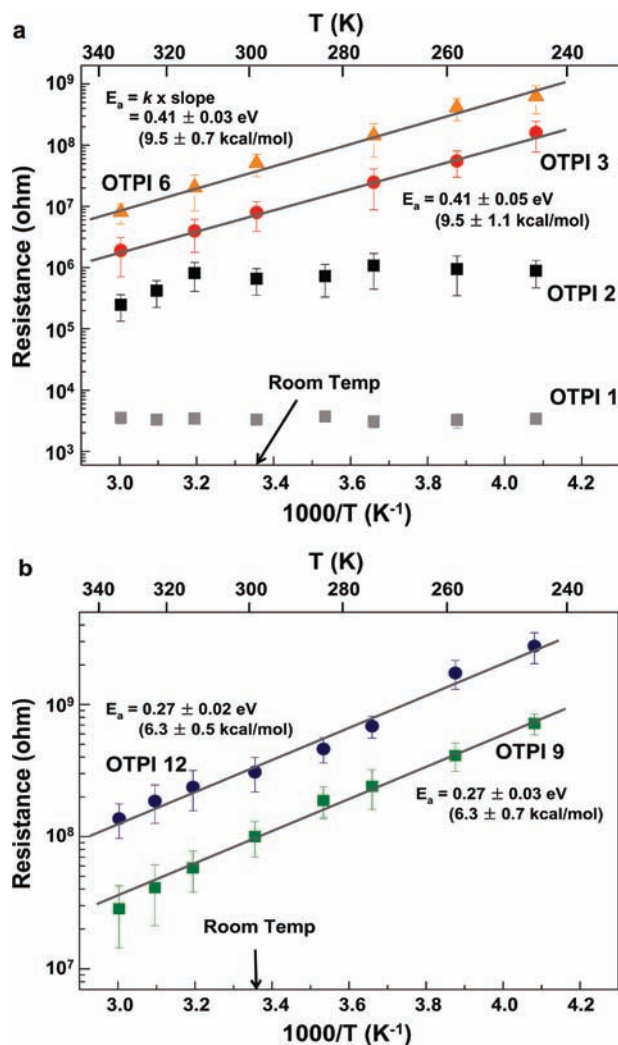


Figure 6. Arrhenius plot for (a) OTPI 1, 2, 3, and 6 and (b) OTPI 9 and 12. Each data point is the average differential resistance obtained at six different locations of samples in the range -1.0 to $+1.0$ mV for OTPI 1 and 2, -0.05 to $+0.05$ V for OTPI 3, 6, 9, and 12. Error bars represent one standard deviation. Straight lines are linear fits to the data.

energy for the two length regimes may reflect changes in the nature of the charge carriers or the conduction process. We anticipate that carriers injected onto the OTPI backbones form polarons, but the size of these polarons (the extent of bond length alteration) and their formation energies are not known. It seems plausible, however, that the carriers themselves, or their hopping mobilities, could be a function of wire length, which would lead to changes in activation energy with wire length. More experiments are required to address this point. Importantly, the differences in charge transport mechanisms in the two length regimes are also manifested in I - V characteristics, which will be discussed in the next section.

We note that the transport activation energies for OTPI wires are significantly reduced (by 70–160 meV) in comparison with our previously reported oligophenylene imine and oligofluorenenaphthalene imine wires ($E_a = 0.54$ – 0.64 eV).^{7,19} The lowering of the hopping energy can be explained as a consequence of the more planar conformation and greater electronic delocalization for OTPI wires relative to the prior examples. Indeed, earlier experimental and theoretical work has shown that donor–acceptor molecules are quite planar with extensive

electronic delocalization.^{64–67} These prior findings are in keeping with our current results.

Electrical Characterization of OTPI Wires (High Bias). So far, the discussion has focused on the length and temperature dependence of the low bias resistance of the wires. To have a complete understanding of transport in a molecular wire, it is also necessary to characterize the conductance over larger voltage ranges. Previously, we have shown the utility of plotting I versus electric field E ,^{7,19} and we present the data here in this manner initially.

Figure 7a–c displays semilog plots of I versus E for OTPI 1–3, 3–6, and 7–12, respectively. Figure 7d combines the data shown in (b) and (c). Comparison of these panels reveals different behavior. For the shortest wires, Figure 7a, the current at any given field decreases strongly with molecular length. However, in Figure 7b and c, the I - E traces collapse nearly on top of one another. This indicates that for the long wires transport is field driven, as expected for a hopping mechanism in which the electric field pushes the carriers along the molecules. On the other hand, for the short wires, the I - E curves do not collapse on top of one another because tunneling is a voltage driven process. Thus, the change in transport mechanism with length is also clearly manifested in the I - E behavior.

In addition, more subtle but important differences in the log I versus E plots are exhibited for two length regimes, that is, regime 1, OTPI 3–6 (5–10 nm) in Figure 7b, and regime 2, OTPI 7–12 (10–20 nm) in Figure 7c. Regime 2 has a more narrowly shaped log I - E trace than regime 1, which indicates that currents in the longest wires are more sensitive to the electric field. This means that the conductivity of the longest wires is greater than the conductivity of the intermediate length wires (because $I = A\sigma E$, where A is the junction area and σ is the bias-dependent conductivity). This point is directly evident in Figure 7d, which overlays the I - E data from panels b and c. One can see that the current at larger E values is higher for the long wires than for the intermediate length wires! We have compared the conductivity in two length regimes (regimes 1 and 2) at different fields (see Figure S3). At high fields (~ 1 MV/cm), the conductivity of the longest wires (regime 2) is ~ 1.2 S/cm, while it is 0.75 S/cm for the regime 1 wires. The higher conductivity for regime 2 wires parallels the smaller hopping energy in Figure 6. That is, the longest wires have smaller transport activation energies than the intermediate length (regime 1) wires and consequently higher conductivities. More work will need to be done to understand why the high field conductivity of the longest wires is greater. However, the UV–vis data indicated that the band gap of the wires continued to decrease with increasing wire length. Smaller band gaps result in more carriers at thermal equilibrium, but this would impact conductivity at all field strengths. It is also clear from Figure 4 that the peak absorption of the wires moves closer to the 680 nm laser diode emission in the CP-AFM apparatus as the wire length increases. This suggests then that the longer wires may have enhanced photoconductivity in the apparatus,

(64) Zhang, Q. T.; Tour, J. M. *J. Am. Chem. Soc.* **1997**, *119*, 5065–5066.

(65) Pai, C.-L.; Liu, C.-L.; Chen, W.-C.; Jenekhe, S. A. *Polymer* **2006**, *47*, 699–708.

(66) Qin, R.; Li, W.; Li, C.; Du, C.; Veit, C.; Schleiermacher, H.-F.; Andersson, M.; Bo, Z.; Liu, Z.; Ingnas, O.; Wuerfel, U.; Zhang, F. *J. Am. Chem. Soc.* **2009**, *131*, 14612–14613.

(67) Janzen, D. E.; Burand, M. W.; Ewbank, P. C.; Pappenfus, T. M.; Higuchi, H.; da Silva Filho, D. A.; Young, V. G.; Bredas, J.-L.; Mann, K. R. *J. Am. Chem. Soc.* **2004**, *126*, 15295–15308.

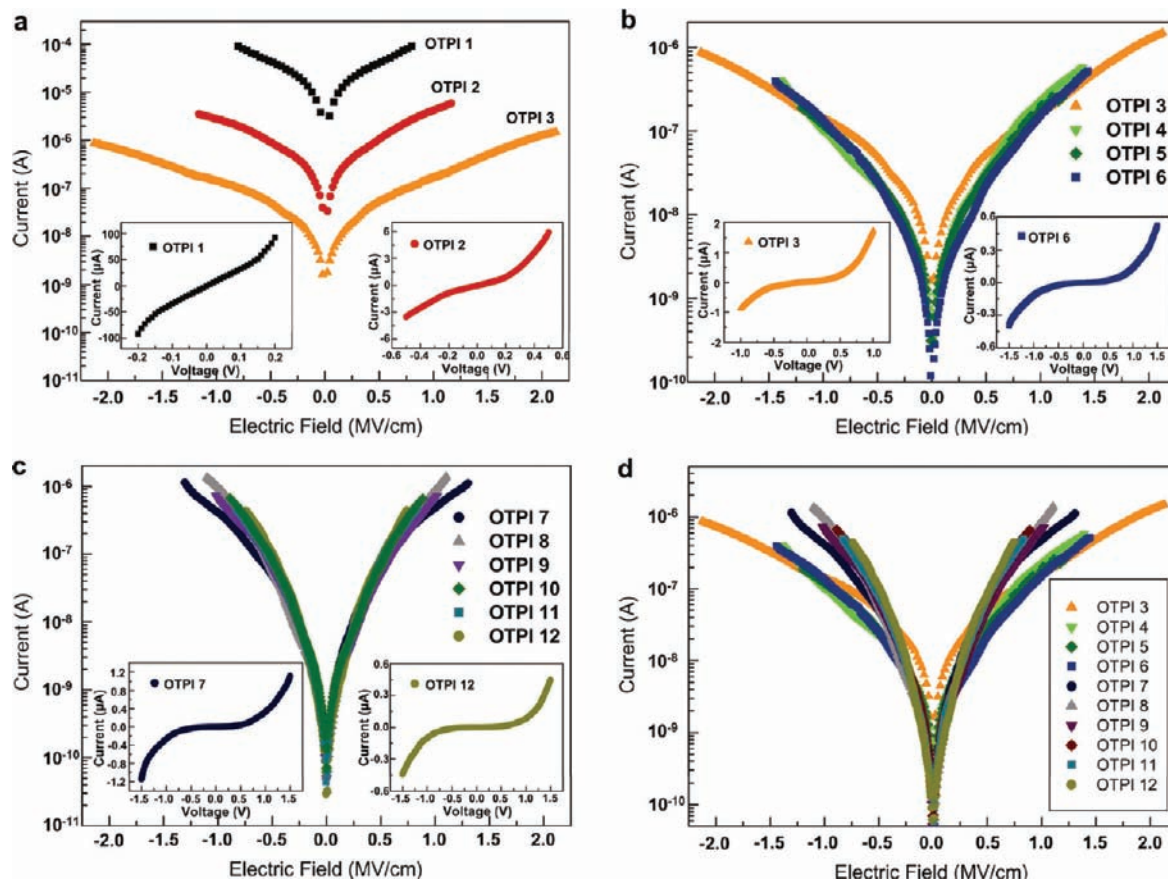


Figure 7. Semilog plot of the average current of 20 I – E traces (a) for Au/short wire/Au junctions, (b) for Au/intermediate wire (regime 1)/Au junctions, (c) for Au/long wires (regime 2)/Au junctions, and (d) for Au/wire (regimes 1 and 2)/gold junctions. The I – E trace for a Au/OTPI 3/Au junction is included in (a) in the comparison with relative current levels of other long wires. The insets are I – V curves in a linear scale for the selected wires of each figure.

particularly at larger fields, which would explain the difference in the I – E curves.

The insets in Figure 7 display the I – V curves for selected wires. All of them are sigmoidally shaped, but there are differences in the symmetry, and also quantitative differences in the transition from low to high voltages. For I – V curves for short wires, a symmetric curve is observed for OTPI 1 (incorporating only one TTF unit), while OTPI 2 (incorporating both TTF and PMDI) shows asymmetric behavior with a current rectification ratio at ± 0.5 V of ~ 2 (that is, current flows more for positive bias on the tip). For OTPI 2, the asymmetry likely arises from intramolecular energy level offsets and not from asymmetries in the contacts, but further increase of wire lengths yields less distinct asymmetry in I – V curves (i.e., rectification is ~ 1.5 for OTPI 6 at ± 0.5 V), and the I – V curves become totally symmetric for the longest wires (OTPI 7–12). Asymmetries in I – V curves are well-known in donor–acceptor molecules as first predicted by Aviram and Ratner⁶⁸ and measured later by Metzger and colleagues.⁶⁹

Figure 8 displays a log–log plot of the I – V characteristics for OTPI 2 and OTPI 12, representative of short and long OTPI wires. From such a plot, one can discern different transport regimes as a function of voltage. At low biases, $I \propto V$ for both OTPI 2, where the transport mechanism is tunneling, and OTPI 12, where the mechanism is hopping.

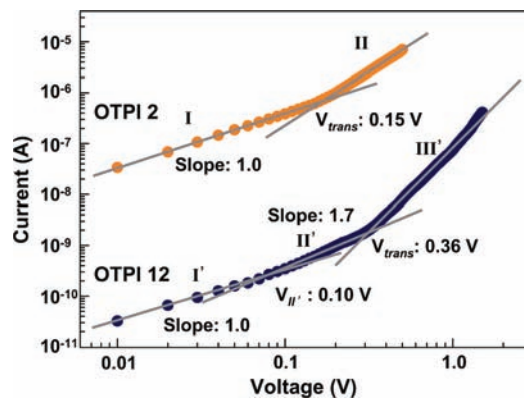


Figure 8. Log–log plot of the average of 20 I – V traces for OTPI 2 and OTPI 12. Fits are shown in the different transport regimes.

It should be noted that linear dependence of I on V is expected for both tunneling and hopping mechanisms at low bias.^{14,18} However, as voltage increases, the slopes of the log–log plots change. In the case of OTPI 2, the transition voltage, V_{trans} , between the two apparent power law domains I and II corresponds to the point where the applied bias becomes comparable to the tunneling barrier height.⁵⁸ The precise

(68) Avram, A.; Ratner, M. *Chem. Phys. Lett.* **1974**, *29*, 277–283.

(69) Metzger, R. M. *Chem. Rev.* **2003**, *103*, 3803–3834.

Table 2. Key Parameters Extracted from the I – V Characteristics for OTPI Wires

monolayer	n in I, I'	n in II'	n in III'	V_{trans} (V) [E_{trans} (MV/cm)]	V_{II} (V) [E_{II} (MV/cm)]
OTPI 1	1.0			0.15 [0.60]	
OTPI 2	1.1			0.16 [0.43]	
OTPI 3	1.0	1.8	3.1	0.49 [0.93]	0.13 [0.25]
OTPI 4	1.1	1.7	2.8	0.35 [0.49]	0.11 [0.15]
OTPI 5	1.0	1.6	2.6	0.34 [0.41]	0.11 [0.13]
OTPI 6	1.1	1.5	2.8	0.35 [0.34]	0.08 [0.08]
OTPI 7	1.1	1.8	3.0	0.28 [0.24]	0.07 [0.06]
OTPI 8	1.0	2.1	3.7	0.36 [0.26]	0.08 [0.06]
OTPI 9	1.1	1.7	3.5	0.37 [0.25]	0.09 [0.06]
OTPI 10	1.0	1.6	3.7	0.39 [0.23]	0.09 [0.05]
OTPI 11	0.9	1.6	3.4	0.37 [0.21]	0.08 [0.04]
OTPI 12	1.1	1.7	3.5	0.36 [0.18]	0.10 [0.05]

interpretation of V_{trans} in the tunneling regime is still being debated and is not our focus here.^{55,58,70}

In the case of OTPI 12, the log–log plot is somewhat more complex. There is a clear slope change at $V_{\text{trans}} = 0.36$ V, but there is also another slope change at lower bias ($V_{\text{II}} = 0.1$ V). Thus, we have indicated three different domains I', II', and III' for OTPI 12. In general, the current scales as V^n , and the values of n and the transition voltages have been tabulated in Table 2 for all OTPI wires. The nature of the mechanistic changes as voltage increases is not clear at this time for the long OTPI wires. In analogy with two terminal measurements on conventional semiconductors, there may be a transition to space charge limited current (SCLC) at higher biases. The theory of SCLC predicts that current will scale with V^2/L^3 , where L is the molecular length.^{71,72} Analysis of the length dependence of the current (and indeed the V dependence also) has not yielded a clear-cut identification of an SCLC transport regime (see Figure S4). The presence of traps or imperfections in the wires could also complicate the analysis and change the precise power law exponents. More experimental and theoretical work must be done to determine the cause of the behavior shown in Figure 8 for OTPI 12.

A natural approach to analyze the mechanistic transitions in long wires is to examine the temperature dependence. Figure 9a displays the I – V characteristics for OTPI 12 as a function of temperature from 245 to 333 K. Current is clearly suppressed at any given voltage as the temperature decreases, which is consistent with the activated transport at low bias that was described earlier. The same data are plotted on log axes in Figure 9b. One sees as in Figure 8 that there are different transport regimes as a function of voltage. We have prepared Arrhenius plots of the current data at selected voltages (see inset). The activation energy for the current is a decreasing function of voltage trending from 0.3 eV at 0.05 V to 0.2 eV at 0.46 V. The decrease in E_a with voltage is broadly consistent with hopping transport and established mobility models, such as the Poole–Frenkel hopping transport model.⁷³ That is, the applied electric field can assist the hopping process: the larger is the electric field, the smaller is the required thermal activation energy. A detailed understanding of the field and temperature

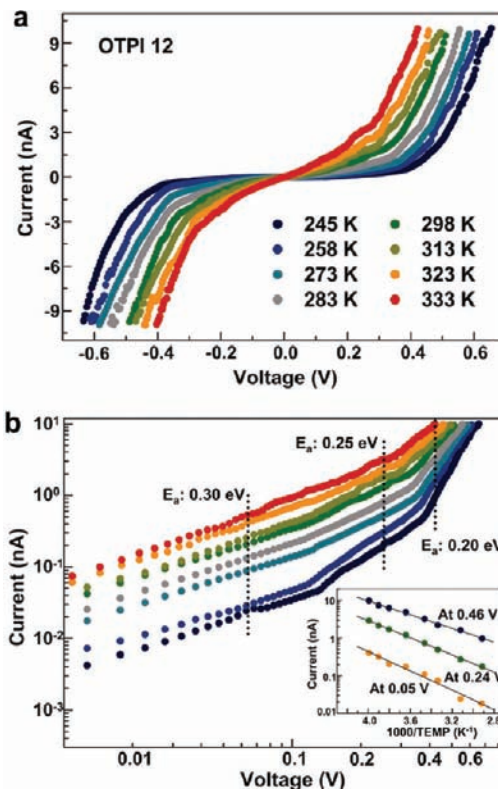


Figure 9. Temperature-dependent I – V characteristics for OTPI 12 on (a) linear axes and (b) log–log axes. Inset in (b) shows Arrhenius plots in three different domains (I', II', III').

dependence of conduction will require further experiments and theoretical modeling.

Conclusion

To summarize, DC electrical conduction has been measured in a set of conjugated alternating donor–acceptor oligoimine wires having systematically controlled lengths between 2.5 and 20.2 nm. These wires incorporate TTF and PMDI as alternating donor/acceptor building blocks and are built from one Au electrode using stepwise aryl imine addition chemistry. At low bias voltages, we have found that the predicted transition from tunneling to hopping transport is exhibited at a molecular length of 5 nm, as supported by mutually consistent changes of the length, temperature, and electric field dependence of the transport characteristics. We have also observed that the donor–acceptor architecture yields enhanced wire conductivity (2 orders of magnitude higher than previous wires^{7,19}). The OTPI wires described here, up to 20 nm in length, are the longest wires for which extensive electrical measurements have been reported.

Detailed examination of the I – E characteristics reveals that the longest chains actually have higher conductivities at high fields than intermediate length chains; this is tentatively ascribed to photoconductivity of the long wires that can absorb the 680 nm laser light used in the CP-AFM apparatus. It is also apparent from the I – V (or I – E) characteristics that the transport mechanism is a function of applied bias (or field), and more work will need to be done to determine the precise mechanisms involved. Future work will also be directed at elucidating the role of intermolecular interactions. Overall, the flexibility of the imine wire synthesis

(70) Huisman, E. H.; Guedon, C. M.; van Wees, B. J.; van der Molen, S. J. *Nano Lett.* **2009**, *9*, 3909–3913.

(71) Rose, A. *Phys. Rev.* **1955**, *97*, 1538–1544.

(72) Lampert, M. A. *Phys. Rev.* **1956**, *103*, 1648–1656.

(73) Sze, S. M. *Physics of Semiconductor Devices*, 2nd ed.; John Wiley & Sons, Inc.: New York, 1981; Chapter 7.

chemistry, its tolerance for a wide range of functionalities, and its utility in synthesizing very long conjugated systems anchored to metals, combined with the soft-contact CP-AFM conductance method, create exciting opportunities for improving fundamental understanding of hopping transport in long conjugated molecules with tunable architectures.

Acknowledgment. This work was supported primarily by the National Science Foundation under CHE-0616427. Partial support for facilities was provided by the NSF MRSEC program under Award Number DMR-0819885. Parts of this work were carried out in the Institute of Technology Characterization Facility,

University of Minnesota, which receives partial support from NSF through the NNIN program.

Supporting Information Available: SI file includes the complete list of authors for ref 24 and supporting figures for wire synthetic route and RIAS spectra up to 12 repeats of OTPI wires, temperature-dependent I – V curves, a plot of wire conductivity (σ) versus voltage, and a log–log plot of I versus L . This material is available free of charge via the Internet at <http://pubs.acs.org>.

JA1060142